

# Detection of Fe and Ti on the dayside of the ultrahot Jupiter MASCARA-1b with CARMENES

B. Guo<sup>1,2</sup>, F. Yan<sup>1,2</sup>, L. Nortmann<sup>2</sup>, D. Cont<sup>3,4</sup>, A. Reiners<sup>2</sup>, E. Pallé<sup>5,6</sup>, D. Shulyak<sup>7</sup>, K. Molaverdikhani<sup>3,8,9</sup>,  
Th. Henning<sup>8</sup>, G. Chen<sup>10,11</sup>, M. Stangret<sup>12</sup>, S. Czesla<sup>13,14</sup>, F. Lesjak<sup>2</sup>, M. López-Puertas<sup>7</sup>, I. Ribas<sup>15,16</sup>,  
A. Quirrenbach<sup>9</sup>, J. A. Caballero<sup>17</sup>, P. J. Amado<sup>7</sup>, M. Blazek<sup>18</sup>, D. Montes<sup>19</sup>, J. C. Morales<sup>15,16</sup>, E. Nagel<sup>2</sup>, and  
M. R. Zapatero Osorio<sup>17</sup>

<sup>1</sup> Department of Astronomy, University of Science and Technology of China, Hefei 230026, China  
e-mail: yanfei@ustc.edu.cn

<sup>2</sup> Institut für Astrophysik und Geophysik, Georg-August-Universität, Friedrich-Hund-Platz 1, 37077 Göttingen, Germany

<sup>3</sup> Ludwig-Maximilians-Universität, Universitäts-Sternwarte München, Scheinerstr. 1, 81679, Munich, Germany

<sup>4</sup> Exzellenzcluster Origins, Boltzmannstraße 2, 85748 Garching, Germany

<sup>5</sup> Instituto de Astrofísica de Canarias (IAC), Vía Lactea s/n, 38200 La Laguna, Tenerife, Spain

<sup>6</sup> Departamento de Astrofísica, Universidad de La Laguna, 38026 La Laguna, Tenerife, Spain

<sup>7</sup> Instituto de Astrofísica de Andalucía - CSIC, Glorieta de la Astronomía s/n, 18008 Granada, Spain

<sup>8</sup> Max-Planck-Institut für Astronomie, Königstuhl 17, 69117 Heidelberg, Germany

<sup>9</sup> Landessternwarte, Zentrum für Astronomie der Universität Heidelberg, Königstuhl 12, 69117 Heidelberg, Germany

<sup>10</sup> CAS Key Laboratory of Planetary Sciences, Purple Mountain Observatory, Chinese Academy of Sciences, Nanjing 210023, China

<sup>11</sup> CAS Center for Excellence in Comparative Planetology, Hefei 230026, China

<sup>12</sup> INAF – Osservatorio Astronomico di Padova, Vicolo dell’Osservatorio 5, 35122, Padova, Italy

<sup>13</sup> Thüringer Landessternwarte Tautenburg, Sternwarte 5, 07778 Tautenburg, Germany

<sup>14</sup> Hamburger Sternwarte, Universität Hamburg, Gojenbergsweg 112, 21029 Hamburg, Germany

<sup>15</sup> Institut de Ciències de l’Espai (CSIC-IEEC), Campus UAB, c/ de Can Magrans s/n, 08193 Bellaterra, Barcelona, Spain

<sup>16</sup> Institut d’Estudis Espacials de Catalunya (IEEC), 08034 Barcelona, Spain

<sup>17</sup> Centro de Astrobiología (CSIC-INTA), ESAC, Camino Bajo del Castillo s/n, E-28692 Villanueva de la Cañada, Madrid, Spain

<sup>18</sup> Centro Astronómico Hispano-Alemán (CSIC-Junta de Andalucía), Observatorio Astronómico de Calar Alto, Sierra de los  
Filabres, 04550 Gérgal, Almería, Spain

<sup>19</sup> Departamento de Física de la Tierra y Astrofísica and IPARCOS-UCM (Instituto de Física de Partículas y del Cosmos de la UCM),  
Facultad de Ciencias Físicas, Universidad Complutense de Madrid, 28040, Madrid, Spain

Received –; accepted –

## ABSTRACT

Ultrahot Jupiters are a type of gaseous exoplanet that orbit extremely close to their host star, resulting in significantly high equilibrium temperatures. In recent years, high-resolution emission spectroscopy has been broadly employed in observing the atmospheres of ultrahot Jupiters. We used the CARMENES spectrograph to observe the high-resolution spectra of the dayside hemisphere of MASCARA-1b in both visible and near-infrared. Through cross-correlation analysis, we detected signals of Fe I and Ti I. Based on these detections, we conducted an atmospheric retrieval and discovered the presence of a strong inversion layer in the planet’s atmosphere. The retrieved Ti and Fe abundances are broadly consistent with solar abundances. In particular, we obtained a relative abundance of [Ti/Fe] as  $-1.0 \pm 0.8$  under the free retrieval and  $-0.4^{+0.5}_{-0.8}$  under the chemical equilibrium retrieval, suggesting the absence of significant titanium depletion on this planet. Furthermore, we considered the influence of planetary rotation on spectral line profiles. The resulting equatorial rotation speed was determined to be  $4.4^{+1.6}_{-2.0}$  km s<sup>-1</sup>, which agrees with the rotation speed induced by tidal locking.

**Key words.** planets and satellites: atmospheres – techniques: spectroscopic – planets and satellites: individuals: MASCARA-1b

## 1. Introduction

Ultrahot Jupiters (UHJs) are giant gas planets that are exceptionally close to their host stars, which results in very high equilibrium temperatures ( $T_{\text{eq}} > 2000$  K). These planets generally exhibit a temperature inversion on their dayside. This is due to the strong absorption of radiation from the star by certain chemical species in the atmosphere, such as iron, hydrogen, TiO, and VO (e.g., Hubeny et al. 2003; Fortney et al. 2008; Lothringer et al. 2018; Muñoz & Schneider 2019; Fossati et al. 2021), which

leads to an increase in temperature in the upper atmospheric layers.

Over the past several years, numerous studies have been conducted to investigate the atmospheres of UHJs using high-resolution emission spectroscopy. For example, in the dayside atmosphere of KELT-20b/MASCARA-2b, chemical species like Fe I, Si I, Fe II, Cr I, and Ni I have been detected (e.g., Yan et al. 2022b; Cont et al. 2022b; Borsa et al. 2022; Johnson et al. 2023; Kasper et al. 2022). Similarly, in the case of KELT-9b, Fe I, Mg I, Si I, and Ca II have been successfully detected using high-resolution spectrometers such as HARPS-N, CARMENES, and

MAROON-X (e.g., Pino et al. 2020; Kasper et al. 2021; Pino et al. 2022; Ridden-Harper et al. 2023). Fe I, Si I, V I, Ti I, CO, OH, and TiO have been detected in WASP-33b (e.g., Nugroho et al. 2020; Cont et al. 2021; Nugroho et al. 2021; Herman et al. 2022; Cont et al. 2022a,b; Yan et al. 2022a; van Sluijs et al. 2023), and the latest research has measured the mixing ratios of CO, H<sub>2</sub>O, and OH, indicating that H<sub>2</sub>O on the dayside is almost completely photodissociated (Finnerty et al. 2023). In addition, the dayside atmospheres of WASP-18b, WASP-76b, WASP-189b, and WASP-121b have also been probed with high-resolution spectroscopy (e.g. Yan et al. 2023; Hoeijmakers et al. 2022; Brogi et al. 2023).

In this paper, we present the detection of Fe I and Ti I in the thermal emission spectrum from the dayside of MASCARA-1b along with the retrieval of the atmospheric properties. The planet MASCARA-1b was discovered by Talens et al. (2017) and orbits a bright and rapidly rotating A8-type star with a period of 2.18 days. With a mass of  $3.7 M_J$  and a radius of  $1.5 R_J$ , the planet has a density similar to that of Jupiter. It has one of the highest densities of the known UHJs. Furthermore, this planet exhibits a surface equilibrium temperature of  $T_{eq} = 2594.3^{+1.6}_{-1.5}$  K (Hooton et al. 2022), placing it among the hottest and most radiative exoplanets known.

There are several previous studies on the atmosphere of MASCARA-1b. Spitzer and CHEOPS observations reveal that MASCARA-1b has a near-polar orbit and uncovers a hint of dayside reflection (Hooton et al. 2022). Some previous studies have also used ESPRESSO (Casasayas-Barris et al. 2022) and HARPS-N (Stangret et al. 2022) to observe its transmission spectrum, but unfortunately no atmospheric signals were detected. This may be due to its high surface gravity ( $\log g = 3.63$  cgs), which results in low scale height, thereby limiting the applicability of high-resolution transmission spectroscopy to MASCARA-1b. However, due to the high integrated dayside temperature of the planet ( $T_{day} = 3062^{+66}_{-68}$  K; Hooton et al. 2022) and the brightness of the host star, we can better study its atmosphere through emission spectroscopy. The PEPSI Exoplanet Transit Survey detected signals of Fe I, Ti I, and Cr I (Scandariato et al. 2023) in its dayside atmosphere, while the high-resolution infrared spectroscopy of CRIRES+ detected signals of CO, H<sub>2</sub>O, and Fe I, confirming the consistency of C/O with the solar value (Ramkumar et al. 2023).

The paper is organized as follows. In Sect.2, we describe the observations and data reduction. In Sect.3, we present the method of atmospheric detection. In Sect.4, we show the detection results. Our atmosphere retrieval method and results are described in Sect.5. The conclusion is presented in Sect.6.

## 2. Observations and data reduction

We observed MASCARA-1b for two nights with the CARMENES spectrograph (Quirrenbach et al. 2018) installed at the 3.5 m telescope of the Calar Alto Observatory. The spectrograph has two channels that cover 520–960 nm in the visible (VIS) with a resolution of 94 600 and 960–1710 nm with a resolution of 80 400 in the near-infrared (NIR). The first observation was performed on the night of August 4, 2020 at orbital phases before the planetary secondary eclipse (program ID: F20-3.5-019). The second observation was performed on the night of August 7, 2022 at orbital phases after the secondary eclipse as part of the CARMENES Legacy program. We observed the target with the VIS and NIR channels simultaneously. The first observing night was interrupted by a cloud passing by and was paused for about one hour. The observation of

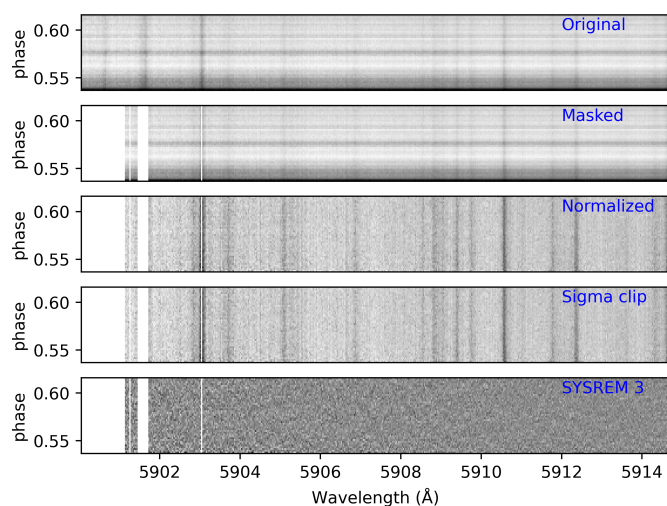


Fig. 1: Example of the data reduction procedure. These are spectra from the second night. The original spectrum, masked spectrum, normalized spectrum, spectrum after the  $5\sigma$  clip, and spectrum after the third SYSREM iteration are presented from top to bottom, respectively.

the second night was performed continuously. The detailed observing logs are presented in Table 1.

The raw data were reduced using the CARMENES pipeline CARACAL (Zechmeister et al. 2014; Caballero et al. 2016). The pipeline handles standard data reduction procedures including dark subtraction, flat fielding, wavelength calibration, and spectrum extraction. The pipeline delivers extracted one-dimensional spectra in the observer’s rest frame that contain 61 spectral orders in the VIS and 28 spectral orders in the NIR. The noise value for each data point of the spectrum is also delivered by the pipeline.

The original spectrum was cleaned to mitigate the influence of significant noise in certain data points. We masked the wavelength points with a low signal-to-noise ratio (S/N) for all the spectra. In the case of VIS data, wavelength points with an S/N of  $< 40$  were masked, while for NIR data, data points with S/N  $< 30$  on the first night and S/N  $< 40$  on the second night – about 20% of the total data points – were masked. Additionally, data points with wavelengths below 5450 Å and above 8920 Å were removed for the VIS data. For the NIR data, spectra from Echelle orders 45–43, which correspond to the strong water absorption band around  $1.4 \mu\text{m}$ , were excluded. We normalized the spectra for each order using a seventh-order polynomial fit. Subsequently, to eliminate potential outliers, such as strong sky emission lines, a  $5\sigma$  clip was applied to each order as an additional step.

The SYSREM algorithm (Tamuz et al. 2005) was employed to effectively eliminate both the telluric and stellar lines from the spectrum. The normalized spectral matrix and accompanying noise were provided as inputs to the SYSREM algorithm. The noise was computed via error propagation. We ran SYSREM ten consecutive times on the normalized data, and each time we got a SYSREM model. Then we divided the normalized data by the SYSREM model to get the residual spectral matrix that was finally used for cross-correlation. An example of the data reduction procedure is presented in Fig.1.

Table 1: Observation logs.

	Date	Airmass change	Exposure time (s)	$N_{\text{spectra}}$	Phase coverage	$S/N$ range <sup>(a)</sup>
VIS night-1	2020-08-04	1.67–1.12–1.13	120	66	0.382–0.460	51–85
VIS night-2	2022-08-07	1.22–1.12–1.34	300	42	0.537–0.616	51–105
NIR night-1	2020-08-04	1.67–1.12–1.13	126	68	0.382–0.460	27–61
NIR night-2	2022-08-07	1.22–1.12–1.34	306	42	0.537–0.616	41–72

Notes.<sup>(a)</sup> The  $S/N$  per pixel was measured at  $\sim 6731 \text{ \AA}$  for the VIS data and  $\sim 12678 \text{ \AA}$  for the NIR data.

### 3. Method

#### 3.1. Model spectra

Before performing the cross-correlation, we calculated the corresponding thermal emission spectrum model of MASCARA-1b. Our assumed atmospheric model is as described in Yan et al. (2020). We used a two-point temperature-pressure profile, with the higher altitude point ( $T_1, P_1$ ) set at (4500 K,  $10^{-3}$  bar) and the lower altitude point ( $T_2, P_2$ ) set at (2000 K,  $10^{-1.5}$  bar). Additionally, we assumed constant mixing ratios for each species, matching the metal abundance found in the Sun. For example, the volume mixing ratio was set as  $10^{-4.59}$  for Fe I and  $10^{-7.14}$  for Ti I. The metal opacities were derived from the Kurucz line list (Kurucz et al. 2018); CrH opacities were obtained from the MoL-LIST database (Burrows et al. 2002; Bernath 2020); OH opacities were computed based on the HITEMP line list (Rothman et al. 2010); AlO, FeH, and TiO opacities were sourced from the ExoMol line list (Wende et al. 2010; Patrascu et al. 2015; Tennyson et al. 2016; McKemmish et al. 2019), and VO opacities were calculated using the Plez line list (Mollière et al. 2019). Some other parameters are shown in Table 2. Then we used `petiRADTRANS` (Mollière et al. 2019) to calculate the emission spectrum of the planet ( $F_p$ ), and we assumed that the star's emission spectrum ( $F_s$ ) is a black body radiation spectrum. Since we observed the entire star-planet system and normalized the observed spectra, the final model spectrum was thereby calculated as  $(F_s + F_p)/F_s$ .

#### 3.2. Cross-correlation

We first subtracted the continuum value of unity for both the model spectrum and the residual spectrum. Then we shifted the model spectrum from  $-500 \text{ km s}^{-1}$  to  $500 \text{ km s}^{-1}$  with steps of  $1 \text{ km s}^{-1}$  to generate a grid of spectral templates. The cross-correlation function (CCF) was calculated as

$$\text{CCF} = \sum \frac{r_i m_i}{\sigma_i^2}, \quad (1)$$

where  $r_i$  is the residual spectrum,  $m_i$  is the model spectrum, and  $\sigma_i$  is the noise of the observed spectrum.

The initial CCF was calculated in the observer's rest frame. We subsequently shifted each CCF into the planetary stationary frame with a planetary radial velocity (RV) of

$$v_p = v_{\text{sys}} - v_{\text{bary}} + K_p \sin(2\pi\phi) + \Delta v, \quad (2)$$

where  $v_{\text{sys}}$  is the systemic velocity (shown in Table 2),  $v_{\text{bary}}$  is the barycentric velocity of the observer on the Earth,  $K_p$  is the orbital velocity semi-amplitude,  $\phi$  is the orbital phase,  $\phi = 0$  corresponds to the middle transit time, and  $\Delta v$  is the velocity

Table 2: Parameters of MASCARA-1b.

Parameter	Symbol(unit)	Value
<i>The star</i>		
Effective temperature	$T_{\text{eff}}$ (K)	$7554 \pm 150^{(a)}$
Radius	$R_*$ ( $R_{\odot}$ )	$2.1 \pm 0.2^{(a)}$
Mass	$M_*$ ( $M_{\odot}$ )	$1.72 \pm 0.07^{(a)}$
Systemic velocity	$v_{\text{sys}}$ ( $\text{km s}^{-1}$ )	$11.20 \pm 0.08^{(a)}$
Metallicity	[Fe/H] (dex)	$0.15 \pm 0.15^{(b)}$
<i>The planet</i>		
Radius	$R_p$ ( $R_J$ )	$1.5 \pm 0.3^{(a)}$
Mass	$M_p$ ( $M_J$ )	$3.7 \pm 0.9^{(a)}$
Surface gravity	$\log g$ (log cgs)	$3.63^{+0.29}_{-0.27}$
Inclination	$i_p$ (degree)	$87^{+2}_{-3}^{(a)}$
Orbital period	$P$ (day)	$2.1487738$ $\pm 0.0000009^{(b)}$
Transit epoch	$T_0$ (BJD)	$2458833.48815$ $\pm 0.00009^{(b)}$
Transit duration	$T_{14}$ (hours)	$4.05 \pm 0.03^{(a)}$
RV semi-amplitude	$K_p$ ( $\text{km s}^{-1}$ )	$197.4 \pm 2.7$

References. (a) Talens et al. (2017). (b) Hooton et al. (2022).

deviation from the planetary rest frame. The  $\Delta v$  parameter accounts for the uncertainty of  $v_{\text{sys}}$ ,  $v_{\text{bary}}$  and  $K_p \sin(2\pi\phi)$  and can also serve as an indication of planetary rotation and atmospheric circulation.  $K_p$  and  $\Delta v$  are the unknown quantities that we aim for. The obtained CCF map for Fe I is shown in Fig.2. We repeated this procedure for various  $K_p$  ranges from  $80 \text{ km s}^{-1}$  to  $300 \text{ km s}^{-1}$ . For each  $K_p$ , we summed all CCFs in the planetary frame along the time dimension to obtain a one-dimensional array. By applying the same procedure to each  $K_p$ , we obtained the  $K_p$ - $\Delta v$  map. To obtain an  $S/N$  map of the investigated chemical species, we normalized the  $K_p$ - $\Delta v$  map with an estimate of the noise level, for which we used the average value in the  $K_p$ - $\Delta v$  map, excluding the region around the central peak. The obtained  $S/N$  maps for Fe I and Ti I are shown in Fig.3. An evident signal at the theoretical  $K_p$  and  $\Delta v = 0$  confirms the existence of the chemical species.

### 4. Detection of chemical species

We detected signals of Fe I and Ti I, and the corresponding  $S/N$  map is presented in Fig.3. We chose the SYSREM iteration number that yields the highest significance value on the  $S/N$  map (see Fig.A.1 for Fe I and Fig.A.2 for Ti I). The Fe I signal is relatively strong and can be identified directly on the CCF map (Fig.2). For demonstration purposes, we combined the VIS and NIR CCF

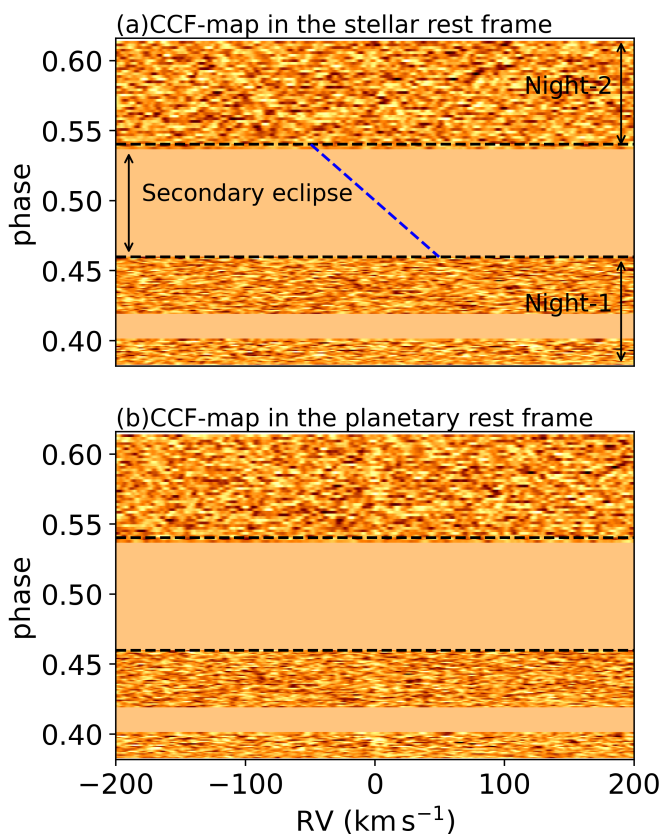


Fig. 2: Cross-correlation functions for Fe I from the two nights. *Upper panel:* CCF map in the stellar rest frame. *Lower panel:* CCF map in the planetary rest frame, which was shifted relative to the stellar rest frame by assuming a theoretical  $K_p$  of  $197.4 \text{ km s}^{-1}$  obtained through Eq.(3). The horizontal dashed lines indicate the beginning and end of the secondary eclipse. The dashed blue line denotes the planetary orbital motion RV.

maps, as is shown in Fig.2. Due to the slight phase difference between the VIS and NIR data, we interpolated the VIS CCF map to a grid of phase values as the NIR data and then directly summed them.

The theoretical  $K_p$  value of MASCARA-1b was calculated to be  $197.4 \pm 2.7 \text{ km s}^{-1}$  using the equation

$$K_p = \left( \frac{2\pi G \cdot M_\star}{P} \right)^{\frac{1}{3}} \cdot \sin i_p, \quad (3)$$

where  $G$  is the gravitational constant,  $P$  is the orbital period,  $M_\star$  is the stellar mass, and  $i_p$  is the orbital inclination. The Fe I signal achieves a maximum S/N ( $\sim 12.1$ ) at  $K_p = 197.9^{+2.5}_{-2.6} \text{ km s}^{-1}$  and  $\Delta v = -1.6 \pm 1.2 \text{ km s}^{-1}$ , aligned with the theoretical  $K_p$  value. Fe I is detected in both VIS and NIR spectra (see Fig.4). The maximum S/N ( $\sim 4.9$ ) for Ti I is located at  $K_p = 199.1^{+3.5}_{-4.2} \text{ km s}^{-1}$  and  $\Delta v = -1.3^{+1.6}_{-1.7} \text{ km s}^{-1}$ , which is consistent with the theoretical  $K_p$  value. Although the Ti I signal is weaker than that of Fe I, Ti I is also detected in both VIS and NIR spectra. All of the detection results are summarized in Table 3.

We also applied the identical method to search for Al I, AlO, Ba I, Ca I, Co I, Cr I, CrH, Fe II, FeH, Li I, Na I, Mg I, Mn I, Sc I, Ti II, TiO, V I, V II, VO, Si I, and OH. Although some tentative signals were detected in some of the data for certain chemical

Table 3: Summary of cross-correlation results.

chemical species	S/N	$K_p$ [km s $^{-1}$ ]	$\Delta v$ [km s $^{-1}$ ]
Fe I	12.05	$197.9^{+2.5}_{-2.6}$	$-1.6 \pm 1.2$
Ti I	4.87	$199.1^{+3.5}_{-4.2}$	$-1.3^{+1.6}_{-1.7}$

species (see Fig.A.3) – for example, the signal of Si I was detected in the NIR data from the first night – the corresponding cross-correlation signals were not obtained when all the observation data were combined. These tentative signals could possibly be random noise. Therefore, we do not claim to have detected any of these chemical species in MASCARA-1b with the CARMENES data. A selection of S/N maps are presented in Fig.A.4, Fig.A.5, Fig.A.6, and Fig.A.7.

The CARMENES detections of Fe I and Ti I are consistent with the previous PEPSI detection by Scandariato et al. (2023); however, we were not able to detect Cr I, which was reported in their work. This may be due to the difference in the wavelength coverage of the two instruments. Compared to PEPSI’s wavelength domain ( $4800 - 5441 \text{ \AA}$  and  $7419 - 9067 \text{ \AA}$ ), the wavelength coverage of CARMENES ( $5200 - 17100 \text{ \AA}$ ) does not contain a significant number Cr I spectral lines, especially after we masked the points with wavelengths below  $5450 \text{ \AA}$  (see Fig.A.4).

The presence of Ti I and V I in the atmosphere of UHJs is of great interest because of the importance of their oxides (i.e., TiO and VO; Hubeny et al. 2003; Fortney et al. 2008). The strong absorption of stellar radiation by TiO and VO has long been believed to be a possible cause of the formation of the temperature inversion layer in the atmosphere of UHJs. However, TiO and VO molecules are not commonly detected in UHJs. Therefore, it is proposed that Ti and V can be cold-trapped on the night-side where the temperature is lower than the condensation temperature of Ti I and V I, which leads to the absence of TiO and VO features in the transmission and emission spectra. In recent years, Ti I depletion phenomena have been discovered on WASP-121b (Hoeijmakers et al. 2022) and WASP-76b (Pelletier et al. 2023). However, we detected Ti I on MASCARA-1b, indicating that there may not be a Ti cold-trap on MASCARA-1b. This may be due to the high equilibrium temperature of MASCARA-1b ( $T_{\text{eq}} = 2594.3^{+1.6}_{-1.5} \text{ K}$ ).

## 5. Retrieval of atmospheric properties

### 5.1. Retrieval method

Atmospheric retrieval techniques for high-resolution spectroscopy were motivated by Brogi & Line (2019), Shulyak et al. (2019), Gibson et al. (2020) and Yan et al. (2020) in recent years. We retrieved the atmospheric properties with the observed emission spectra of Fe I and Ti I, employing the latest retrieval method described in Yan et al. (2023).

Forward models were calculated using `petitRADTRANS`, assuming a two-point  $T$ - $P$  profile for the atmospheric structure. We set the high-altitude temperature,  $T_1$ , and the low-altitude temperature,  $T_2$ , as free parameters. The range of  $T_1$  is from 2000 to 6000 K and the range of  $T_2$  is from 1000 to 5000 K. We defined the pressure point,  $\log P_1$ , at high altitude as a free parameter, ranging from  $-7$  to  $0$  (log bar). Simultaneously, the pressure

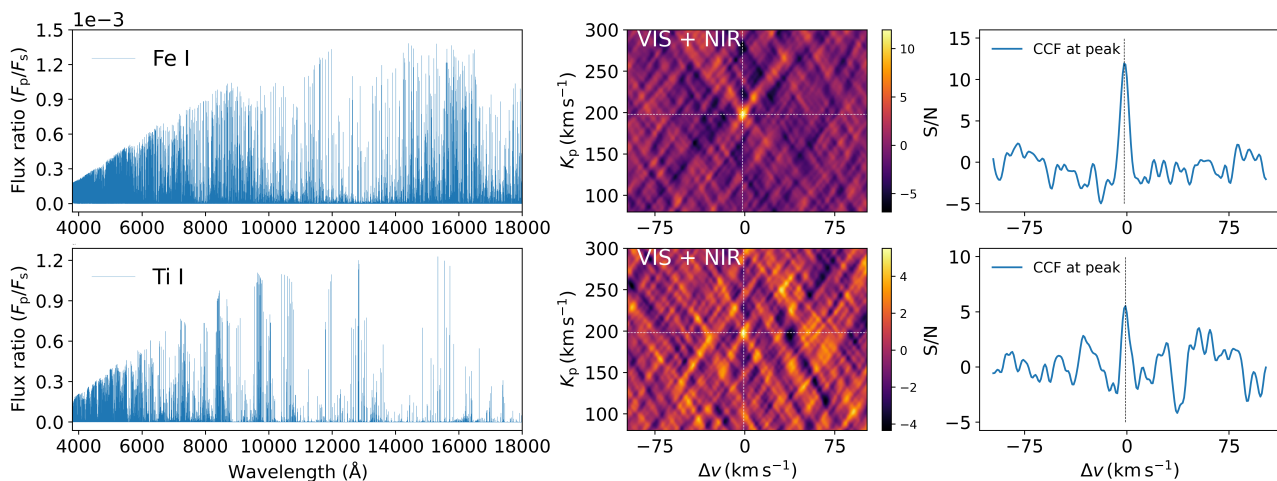


Fig. 3: Model spectra and S/N maps of Fe I and Ti I. *Left panels:* Model spectrum of each chemical species. *Middle panels:* S/N map of each chemical species. The signals from both the VIS and NIR channels are combined. The dotted white line is the position of  $K_p - \Delta v$  where the S/N is maximum. *Right panels:* CCF at the  $K_p$  of the maximum S/N.

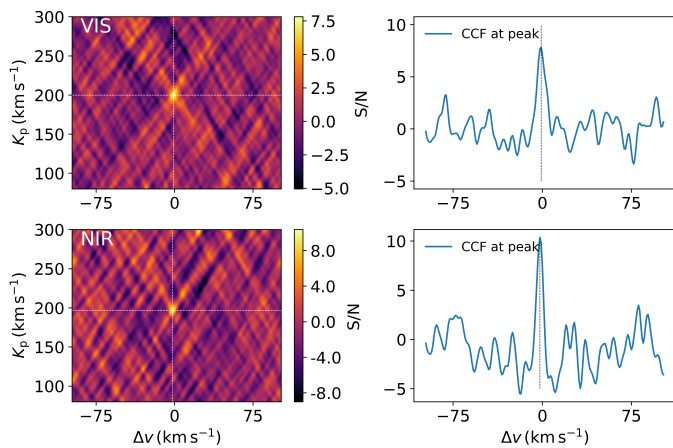


Fig. 4: S/N maps of Fe I from the VIS channel (upper panels) and the NIR channel (lower panels).

difference,  $dP$ , between high and low altitude points was utilized to indirectly represent the pressure at low altitude ( $\log P_2 = \log P_1 + dP$ ). The value of  $dP$  is also a free parameter, varying between 0 and +7. Since  $dP$  was set as  $> 0$ , we ensured that  $P_2$  is always at a higher pressure than  $P_1$ . We set the atmosphere structure in `petitRADTRANS` as 25 pressure layers, evenly spaced in  $\log(P)$  from 1 bar to  $10^{-8}$  bar. Such a setup means that the lower boundary of the atmosphere is set at 1 bar. Then we generated a model spectral matrix with the same data structure as the observed residual spectral matrix. The model spectra were translated into the observer's stationary frame using the RV value described in Eq.(2).

Regarding the treatment of the mixing ratio of the chemical species, we employed two different methods. The first method was free retrieval, in which the volume mixing ratio of each chemical species is assumed to be constant across all pressure levels of the planetary atmosphere. For example, we denoted the logarithm of the Fe I volume mixing ratio as  $\log(\text{Fe})$ . The second method is chemical equilibrium retrieval. We assumed the elemental abundance of each atom or ion to be a free parameter. For example, the iron elemental abundance ( $[\text{Fe}/\text{H}]$ ) was assumed to be a free parameter in the retrieval. Here,  $[\text{Fe}/\text{H}]$  refers

to the logarithm of the ratio between the Fe/H of the planet and the Fe/H of the Sun. The actual profile of the Fe I mixing ratio was then computed under the chemical equilibrium assumption for given  $[\text{Fe}/\text{H}]$  values. We used the chemical equilibrium module `easyCHEM` of `petitCode` (Mollière et al. 2015, 2017), which consists of 84 chemical species, including Fe I, Fe II, Ti I, Ti II, V I, V II, TiO, VO, and FeH.

In the retrieval process, line profile broadening was also taken into consideration. Pressure and thermal broadening were already accounted during the calculation of the `petitRADTRANS` opacity grid. Additionally, the model spectrum was convolved with the instrumental profile. Gaussian profiles were assumed for the instrumental broadening, with a VIS spectral resolution of  $R = 94\,600$  and a NIR spectral resolution of  $R = 80\,400$ . The `broadGaussFast` code from `PyAstronomy` (Czesla et al. 2019) was used for this convolution. Moreover, the influence of planetary rotation on spectral line broadening was considered. We used the rotational profile in Díaz et al. (2011),

$$G(x) = \frac{2(1 - \varepsilon)(1 - x^2)^{\frac{1}{2}} + \frac{\pi\varepsilon}{2}(1 - x^2)}{\pi(1 - \frac{\varepsilon}{3})}, \quad (4)$$

to calculate the rotational broadening, where  $x = \ln(\lambda/\lambda_0) \cdot c/(v_{\text{eq}} \sin i)$ ,  $\lambda_0$  is the central wavelength of the spectral line,  $\varepsilon$  is the limb darkening coefficient, and  $v_{\text{eq}}$  is the equatorial rotation velocity. We assumed a linear limb darkening model and set  $\varepsilon$  to 1, implying that the radiation from the limb region of the planet does not contribute to the total radiation flux. Since the atmospheric distribution of planets is inhomogeneous,  $\varepsilon$  represents both the limb darkening and the degree of inhomogeneity of the thermal distribution. Finally, we convolved the model spectrum with this rotational profile in velocity space (i.e.,  $\ln \lambda$ ).

During the data reduction process, the observed spectrum underwent the `SYSREM` algorithm, altering the intensity and profile of the planetary lines. The actual distortion of the line profile is also phase-dependent. Therefore, it is theoretically necessary to perform the same `SYSREM` processing on the model matrix before fitting it with the residual spectral matrix. Nevertheless, implementing the `SYSREM` algorithm for each template spectral matrix would be time-consuming. We utilized the fast `SYSREM`

filtering technique described by Gibson et al. (2022) to mitigate this issue. We generated a filter matrix while performing SYSREM on the observed spectral matrix. The filter matrix was generated during the SYSREM process on the observed spectral matrix. The filter matrix was then multiplied with the model spectrum matrix, resulting in the final model spectral matrix. Furthermore, a Gaussian high-pass filter with a Gaussian  $\sigma$  of 31 points was applied to both the final residual matrix and model spectral matrix to remove any remaining broadband features.

We performed the atmospheric retrieval by evaluating the likelihood function with the Markov chain Monte Carlo (MCMC) simulation tool emcee (Foreman-Mackey et al. 2013). The logarithm likelihood function is described as

$$\ln(L) = - \sum_i \left[ \frac{(R_i - \alpha M_i)^2}{(\beta \sigma_i)^2} + \ln(2\pi(\beta \sigma_i)^2) \right], \quad (5)$$

where  $R_i$  is the residual spectral matrix,  $M_i$  is the model spectral matrix,  $\sigma_i$  is the residual noise matrix,  $\alpha$  is the scale coefficient of the model spectrum, and  $\beta$  is the scale factor of the noise. The  $\alpha$  parameter accounts for the uncertainties of the systemic parameters such as  $(R_p/R_s)^2$ . It also accounts for the fact that only part of the dayside hemisphere faces toward the observer at orbital phases other than 0.5. We used the residual spectral matrix corresponding to the best SYSREM iterations from the Fe I detection. We ran the MCMC simulation with 10000 steps and 100 walkers for each free parameter. For the final retrieval results, we burned in initial 2000 steps.

## 5.2. Retrieval results

### 5.2.1. Temperature structure

The retrieval was performed independently for the free retrieval and chemical equilibrium retrieval. Figure 5 illustrates the final retrieved  $T$ - $P$  profiles. The retrieved parameter values are summarized in Table 4 with posterior distributions plotted in Figs.A.8 and A.9. The retrieval results indicate the presence of a strong atmospheric inversion layer with a temperature difference of  $\sim 1700$  K under the free retrieval. We also conducted a retrieval with  $\alpha$  fixed as 1, but there was no significant difference compared to the retrieval results with free  $\alpha$ . Additionally, we computed self-consistent models employing the modified HELIOS code developed by Malik et al. (2017), which incorporates opacities caused by both neutral and singly ionized species, as was proposed by Fossati et al. (2021). A detailed description of the HELIOS model calculation can be found in Yan et al. (2022b). The  $T$ - $P$  profiles from the HELIOS model are presented in Fig. 5 for comparison. The retrieved temperature difference in the inversion layer is similar to the prediction from the HELIOS model. However, the location of the inversion layer (i.e.,  $P_1$  and  $P_2$ ) has a large dynamic range, which is a result of the degeneracy between the location of the inversion layer and the metallicity.

Compared with the retrieved results using CRILES+ data in Ramkumar et al. (2023), we detected a higher altitude of the inversion layer in the atmospheric structure. This discrepancy can be attributed to several factors. First, there exists a certain degeneracy between  $[\text{Fe}/\text{H}]$  and pressure, which has been reported in previous studies (e.g., Yan et al. 2020). In the retrieval process of Ramkumar et al. (2023), there is an excessive constraint

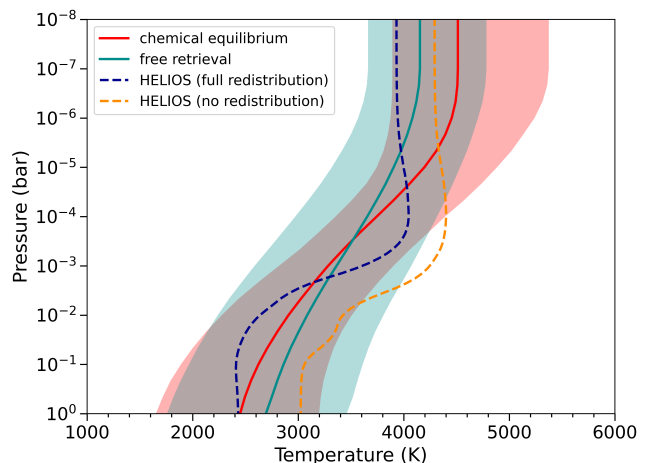


Fig. 5: Retrieved  $T$ - $P$  profile and comparison with the results from the self-consistent HELIOS model. The HELIOS model was calculated assuming solar abundances for both no and full heat redistribution from dayside to nightside. The shadows are the  $1\sigma$  range of the retrieved results.

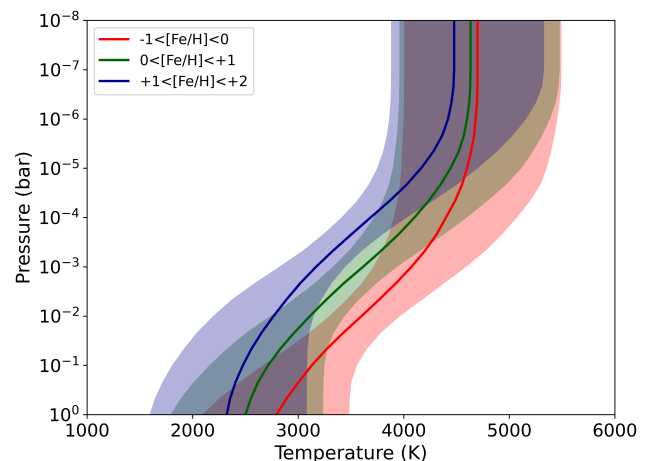


Fig. 6: Retrieved  $T$ - $P$  profile for different  $[\text{Fe}/\text{H}]$  ranges. The shadows are the  $1\sigma$  range of the retrieved results.

on the metallicity  $[\text{M}/\text{H}]$  boundary, hindering its attainment of the optimal fitting value. As a result, the position of the inversion layer can be modified by the strong boundary condition of metallicity. As is shown in Fig.6, if we artificially restrict the range of  $[\text{Fe}/\text{H}]$  to smaller interval, the altitude of the inversion layer will correspondingly change also. When the metallicity is limited to  $-1 < [\text{Fe}/\text{H}] < 0$ , the pressure at the low-altitude point,  $\log P_2$ , is  $-0.3^{+1.6}_{-1.0}$ . As the metallicity increases to  $0 < [\text{Fe}/\text{H}] < +1$ ,  $\log P_2$  shifts to  $-0.9^{+1.3}_{-1.1}$ . For  $+1 < [\text{Fe}/\text{H}] < +2$ , the pressure reduces to  $\log P_2 = -1.6^{+1.6}_{-1.2}$ . Second, the atmospheric structure is predominantly constrained by CO and H<sub>2</sub>O lines in Ramkumar et al. (2023), while our retrieval is mostly driven by Fe I lines.

### 5.2.2. Chemical abundance

The results of the free retrieval indicate that the volume mixing ratios of Fe I ( $\log(\text{Fe})$ ) and Ti I ( $\log(\text{Ti})$ ) are  $-3.6^{+1.6}_{-1.8}$  and

Table 4: Parameter values from the  $T$ - $P$  profile retrieval.

Parameter (Unit)	free retrieval	chemical equilibrium	Boundaries
$T_1$ (K)	$4200^{+600}_{-500}$	$4500^{+900}_{-600}$	2000 to 6000
$\log P_1$ (log bar)	$-5.3^{+2.3}_{-1.2}$	$-5.4^{+1.3}_{-1.0}$	-7 to 0
$T_2$ (K)	$2500^{+800}_{-1000}$	$2300^{+800}_{-900}$	1000 to 5000
dP (log bar)	$4.0^{+2.0}_{-2.2}$	$4.2^{+1.7}_{-1.8}$	0 to +7
$\log P_2$ (log bar)	$-1.0^{+2.3}_{-2.2}$	$-1.2^{+1.6}_{-1.4}$	...
$\beta$	$0.90 \pm 0.0003$	$0.90 \pm 0.00025$	0 to 10
$\alpha$	$1.5^{+1.6}_{-0.8}$	$1.5^{+1.4}_{-0.6}$	0 to 10
$\log(\text{Fe})$	$-3.6^{+1.6}_{-1.8}$	...	-10 to 0
[Fe/H] (dex)	$\sim 1.0^{+1.6(a)}_{-1.8}$	$1.4^{+1.1}_{-1.3}$	-3 to +3
$\log(\text{Ti})$	$-7.1^{+1.8}_{-1.7}$	...	-10 to 0
[Ti/H] (dex)	$\sim 0.0^{+1.8(a)}_{-1.7}$	$0.8^{+1.2}_{-1.5}$	-3 to +3
$\log(\text{V})$	$< -7.7$	...	-10 to 0
$v_{\text{eq}}$ (km s $^{-1}$ )	$4.4^{+1.6}_{-2.0}$	$4.1^{+1.6}_{-1.9}$	0 to 20
$\Delta v$ (km s $^{-1}$ )	$-1.2^{+0.7}_{-0.6}$	$-1.2 \pm 0.5$	-20 to 20
$K_p$ (km s $^{-1}$ )	$199.2^{+1.4}_{-1.5}$	$199.4 \pm 1.2$	180 to 220

**Notes.** <sup>(a)</sup> In free retrieval, [Fe/H] is approximately calculated by assuming that the Fe element exists mainly in the form of Fe I and the atmosphere is mainly composed of H I.

$-7.1^{+1.8}_{-1.7}$ , respectively. Since the actual  $\log(\text{Fe})$  and  $\log(\text{Ti})$  will decrease with altitude due to thermal ionization, the retrieved  $\log(\text{Fe})$  and  $\log(\text{Ti})$  should be considered as average values in the inversion layer. We further computed the elemental abundance of Fe and Ti relative to the Sun using the free retrieval results (see Fig. 7). Here, we assumed that all the Fe and Ti chemical species are in the format of atomic iron and atomic titanium and that the atmosphere is mainly composed of H I. The obtained [Fe/H] has a value  $\sim 1.0^{+1.6}_{-1.8}$  and [Ti/H] has a value  $\sim 0.0^{+1.8}_{-1.7}$ , which are both consistent with the solar metallicity within one  $\sigma$ . We also calculated the relative abundance between Ti and Fe ([Ti/Fe]) using the MCMC samples and obtained [Ti/Fe] as  $-1.0 \pm 0.8$ . While V I was not detected, we obtained its one  $\sigma$  upper limit as  $\log(\text{V}) < -7.7$ . This upper limit is close to the solar vanadium mixing ratio ( $\log(\text{V}) = -8.04$ ), indicating that the non-detection of V I will be attributed to the detection limitation of our data rather than the depletion of vanadium in the atmosphere.

For the chemical equilibrium retrieval, we obtained the [Fe/H] value as  $1.4^{+1.1}_{-1.3}$  and the [Ti/H] value as  $0.8^{+1.2}_{-1.5}$ , which are both consistent with the abundances from the free retrieval. The retrieved relative abundance of [Ti/Fe] is  $-0.4^{+0.5}_{-0.8}$ . The actual mixing ratios of Fe I and Ti I atoms from the chemical equilibrium retrieval are plotted in Fig. 8. At high altitudes, the chemical equilibrium mixing ratios are significantly smaller than the constant mixing ratios from the free retrieval, which is caused by the high thermal ionization rate at low pressures; for example, Fe I dissociates into Fe II in large quantities. At very low altitudes, the chemical equilibrium mixing ratios are also slightly weaker than the free retrieval values. This is because Fe I is partially condensed under high pressures, while the Ti element is

mostly in the form of TiO instead of the Ti I atom at very low altitudes.

Although the chemical equilibrium model includes chemical processes, compared to the free retrieval it also has certain limitations. First, nonlocal thermodynamic equilibrium effects may have some impact on the retrieval results. The presence of the inversion layer leads to higher temperatures in the planet's upper atmosphere. This causes certain energy levels of species such as Fe I in the upper atmosphere to be overpopulated, emitting stronger spectral lines. This can lead to an overestimation of the mixing ratio under the local thermodynamic equilibrium assumption. Second, vertical wind may exist between the lower and upper layers of the atmosphere (Seidel et al. 2021). These vertical winds can be described as outward-expanding winds, which transport substances such as Fe I from the lower atmosphere to the upper atmosphere, forming a vertical material transport in the atmosphere. According to the theory proposed by Moses (2014), if the timescale of transport is shorter than the chemical kinetic timescale required to maintain equilibrium between this component and other species, a component like Fe I may fail to maintain a state of chemical equilibrium. This phenomenon, known as transport-induced quenching, leads to a constant volume mixing ratio for the species instead of the mixing ratio profile predicted by the chemical equilibrium model.

### 5.2.3. Velocity signatures

The retrieved equatorial rotation speed,  $v_{\text{eq}}$ , is  $4.4^{+1.6}_{-2.0}$  km s $^{-1}$  in the free retrieval. If we assume that the planet is tidally locked, the corresponding equatorial rotation speed is 3.55 km s $^{-1}$ .

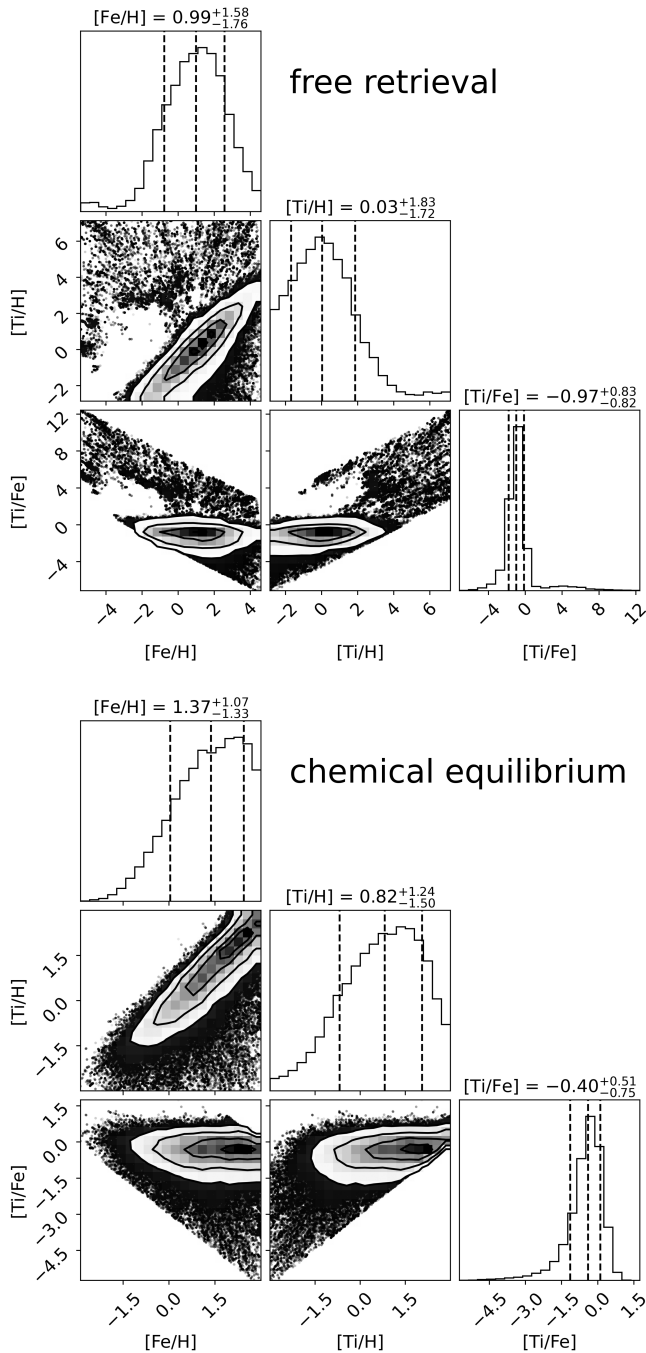


Fig. 7: Element abundances of Fe and Ti relative to the Sun. The upper panel is the result of free retrieval and the lower panel is from chemical equilibrium retrieval.

Therefore, the retrieved  $v_{\text{eq}}$  is in agreement with the tidally locked rotation speed, considering the uncertainty range of the retrieved value. In addition to planetary rotation, atmospheric circulation such as super-rotation also contributes to the line profile; for example, a prominent super-rotation will result in a large  $v_{\text{eq}}$ . Therefore, our retrieved  $v_{\text{eq}}$  hints that the planet may not have a significant equatorial super-rotation jet.

In all of the retrievals,  $K_p$  and  $\Delta v$  were treated as free parameters. The retrieval results indicate that  $K_p$  is approximately  $199 \text{ km s}^{-1}$  and  $\Delta v$  is approximately  $-1 \text{ km s}^{-1}$ , which corroborates the findings from the cross-correlation results. The  $\Delta v$  of

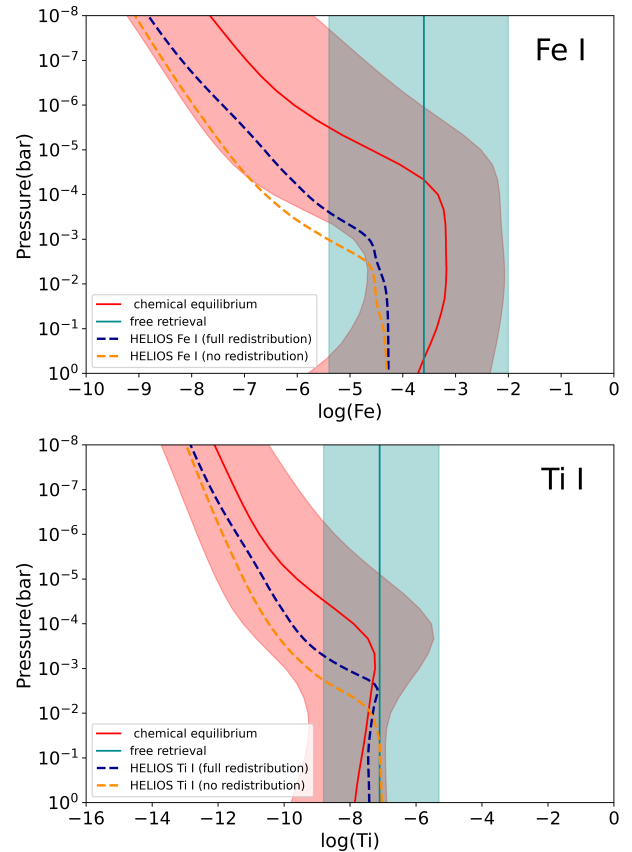


Fig. 8: Retrieved volume mixing ratio of Fe I (upper panel), Ti I (lower panel), and a comparison with the results from the self-consistent HELIOS model. The shaded regions show the  $1\sigma$  range of the retrieved results.

the Fe I signal deviates very slightly from the rest frame of the planet. The blueshift or redshift of the detection signal is normally an indication of planetary rotation and atmospheric circulation. However, there are several other factors that can cause the change in  $\Delta v$ . First, the uncertainty of the transit epoch can lead to the change in  $\Delta v$ . For example, if we were to use an older transit epoch ( $T_0$ ) from Talens et al. (2017), it would result in a deviation of approximately  $-2 \text{ km s}^{-1}$  compared to the RV calculated using the latest measured  $T_0$  from Hooton et al. (2022). Second, Talens et al. (2017) found that the measured stellar systemic velocity varies with different instruments; for example,  $v_{\text{sys}} = 11.20 \pm 0.08 \text{ km s}^{-1}$  for HERMES and  $v_{\text{sys}} = 8.50 \pm 0.02 \text{ km s}^{-1}$  for SONG. Casasayas-Barris et al. (2022) reports a systemic velocity of  $9.3 \pm 2.3 \text{ km s}^{-1}$  measured using ESPRESSO data. This suggests the presence of high uncertainty in the determination of systemic velocity for early-type stars such as MASCARA-1, which in turn leads to high systematic uncertainty of the obtained  $\Delta v$ .

## 6. Conclusions

We observed the emission spectrum of MASCARA-1b before and after the secondary eclipse using the CARMENES spec-

trograph. By employing the cross-correlation technique, we detected strong signals of Fe I and Ti I in the planetary dayside atmosphere. The detected Fe I and Ti I lines are emission lines, indicating the presence of an inversion layer in the atmosphere. We also used the same method to search for other chemical species, including TiO and VO, but failed to detect them.

We performed atmospheric retrieval on the observed Fe I and Ti I lines. We employed two different methods to calculate the mixing ratios of the chemical substances: free retrieval and chemical equilibrium retrieval. The retrieval results indicate the existence of a strong inversion layer in the atmosphere of MASCARA-1b. The retrieved elemental abundances of Fe and Ti are broadly consistent with the solar values. The obtained relative abundance of [Ti/Fe] is  $-1.0 \pm 0.8$  in the free retrieval and  $-0.4^{+0.5}_{-0.8}$  in the chemical equilibrium retrieval, indicating that there is no significant depletion of Ti on this planet. We also considered rotational broadening and obtained an equatorial rotational velocity,  $v_{\text{eq}}$ , of around  $4.4 \text{ km s}^{-1}$ , which agrees with the tidally locked rotation velocity. During the retrieval process, we treated  $K_p$  and  $\Delta v$  as free parameters, and the results were consistent with those obtained from cross-correlation.

*Acknowledgements.* We acknowledge the support by the National Natural Science Foundation of China (grant No. 42375118). This publication was based on observations collected under the CARMENES Legacy+ project. CARMENES is an instrument for the Centro Astronómico Hispano-Alemán (CAHA) at Calar Alto (Almería, Spain), operated jointly by the Junta de Andalucía and the Instituto de Astrofísica de Andalucía (CSIC). The authors wish to express their sincere thanks to all members of the Calar Alto staff for their expert support of the instrument and telescope operation. CARMENES was funded by the Max-Planck-Gesellschaft (MPG), the Consejo Superior de Investigaciones Científicas (CSIC), the Ministerio de Economía y Competitividad (MINECO) and the European Regional Development Fund (ERDF) through projects FICTS-2011-02, ICTS-2017-07-CAHA-4, and CAHA16-CE-3978, and the members of the CARMENES Consortium (Max-Planck-Institut für Astronomie, Instituto de Astrofísica de Andalucía, Landessternwarte Königstuhl, Institut de Ciències de l'Espai, Institut für Astrophysik Göttingen, Universidad Complutense de Madrid, Thüringer Landessternwarte Tautenburg, Instituto de Astrofísica de Canarias, Hamburger Sternwarte, Centro de Astrobiología and Centro Astronómico Hispano-Alemán), with additional contributions by the MINECO, the Deutsche Forschungsgemeinschaft through the Major Research Instrumentation Programme and Research Unit FOR2544 “Blue Planets around Red Stars”, the Klaus Tschira Stiftung, the states of Baden-Württemberg and Niedersachsen, and by the Junta de Andalucía. We acknowledge financial support from the Agencia Estatal de Investigación (AEI/10.13039/501100011033) of the Ministerio de Ciencia e Innovación and the ERDF “A way of making Europe” through projects PID2022-137241NB-C4[1:4], PID2021-125627OB-C31, PID2022-141216NB-I00, and the Centre of Excellence “Severo Ochoa” and “María de Maeztu” awards to the Instituto de Astrofísica de Canarias (CEX2019-000920-S), Instituto de Astrofísica de Andalucía (CEX2021-001131-S) and Institut de Ciències de l'Espai (CEX2020-001058-M). F.L. and L.N. acknowledge the support by the Deutsche Forschungsgemeinschaft (DFG, German Research Foundation) – Project number 314665159. D.S. acknowledges financial support from the project PID2021-126365NB-C21(MCI/AEI/FEDER, UE) and from the Severo Ochoa grant CEX2021-001131-S funded by MCIN/AEI/10.13039/501100011033. D.C. is supported by the LMU-Munich Fraunhofer-Schwarzschild Fellowship and by the Deutsche Forschungsgemeinschaft (DFG, German Research Foundation) under Germany’s Excellence Strategy – EXC 2094 – 390783311.

## References

- Bernath, P. F. 2020, *Journal of Quantitative Spectroscopy and Radiative Transfer*, 240, 106687
- Borsa, F., Giacobbe, P., Bonomo, A., et al. 2022, *Astronomy & Astrophysics*, 663, A141
- Brogi, M., Emeka-Okafor, V., Line, M. R., et al. 2023, *The Astronomical Journal*, 165, 91
- Brogi, M. & Line, M. R. 2019, *The Astronomical Journal*, 157, 114
- Burrows, A., Ram, R., Bernath, P., Sharp, C., & Milsom, J. 2002, *The Astrophysical Journal*, 577, 986
- Caballero, J. A., Guàrdia, J., López del Fresno, M., et al. 2016, in *Proc. SPIE*, Vol. 9910, *Observatory Operations: Strategies, Processes, and Systems VI*, 99100E
- Casasayas-Barris, N., Borsa, F., Palle, E., et al. 2022, *Astronomy & Astrophysics*, 664, A121
- Cont, D., Yan, F., Reiners, A., et al. 2021, *Astronomy & Astrophysics*, 651, A33
- Cont, D., Yan, F., Reiners, A., et al. 2022a, *Astronomy & Astrophysics*, 668, A53
- Cont, D., Yan, F., Reiners, A., et al. 2022b, *Astronomy & Astrophysics*, 657, L2
- Czesla, S., Schröter, S., Schneider, C. P., et al. 2019, *Astrophysics Source Code Library*, ascl
- Díaz, C., González, J., Levato, H., & Grosso, M. 2011, *Astronomy & Astrophysics*, 531, A143
- Finnerty, L., Schofield, T., Sappéy, B., et al. 2023, *The Astronomical Journal*, 166, 31
- Foreman-Mackey, D., Hogg, D. W., Lang, D., & Goodman, J. 2013, *Publications of the Astronomical Society of the Pacific*, 125, 306
- Fortney, J. J., Lodders, K., Marley, M. S., & Freedman, R. S. 2008, *The Astrophysical Journal*, 678, 1419
- Fossati, L., Young, M., Shulyak, D., et al. 2021, *Astronomy & Astrophysics*, 653, A52
- Gibson, N. P., Merritt, S., Nugroho, S. K., et al. 2020, *Monthly Notices of the Royal Astronomical Society*, 493, 2215
- Gibson, N. P., Nugroho, S. K., Lothringer, J., Maguire, C., & Sing, D. K. 2022, *Monthly Notices of the Royal Astronomical Society*, 512, 4618
- Herman, M. K., de Mooij, E. J., Nugroho, S. K., Gibson, N. P., & Jayawardhana, R. 2022, *The Astronomical Journal*, 163, 248
- Hoeijmakers, H., Kitzmann, D., Morris, B., et al. 2022, arXiv preprint arXiv:2210.12847
- Hooton, M. J., Hoyer, S., Kitzmann, D., et al. 2022, *Astronomy & Astrophysics*, 658, A75
- Hubeny, I., Burrows, A., & Sudarsky, D. 2003, *The Astrophysical Journal*, 594, 1011
- Johnson, M. C., Wang, J., Asnodkar, A. P., et al. 2023, *The Astronomical Journal*, 165, 157
- Kasper, D., Bean, J. L., Line, M. R., et al. 2022, *The Astronomical Journal*, 165, 7
- Kasper, D., Bean, J. L., Line, M. R., et al. 2021, *The Astrophysical Journal Letters*, 921, L18
- Kurucz, R., Mendoza, C., Turck-Chièze, S., & Colgan, J. 2018
- Lothringer, J. D., Barman, T., & Koskinen, T. 2018, *The Astrophysical Journal*, 866, 27
- Malik, M., Grosheintz, L., Mendonça, J. M., et al. 2017, *The astronomical journal*, 153, 56
- McKemmish, L. K., Masseron, T., Hoeijmakers, H. J., et al. 2019, *Monthly Notices of the Royal Astronomical Society*, 488, 2836
- Mollière, P., van Boekel, R., Bouwman, J., et al. 2017, *Astronomy & Astrophysics*, 600, A10
- Mollière, P., van Boekel, R., Dullemond, C., Henning, T., & Mordasini, C. 2015, *The Astrophysical Journal*, 813, 47
- Mollière, P., Wardenier, J., Van Boekel, R., et al. 2019, *Astronomy & Astrophysics*, 627, A67
- Moses, J. I. 2014, *Philosophical Transactions of the Royal Society A: Mathematical, Physical and Engineering Sciences*, 372, 20130073
- Muñoz, A. G. & Schneider, P. 2019, *The Astrophysical Journal Letters*, 884, L43
- Nugroho, S. K., Gibson, N. P., de Mooij, E. J., et al. 2020, *The Astrophysical Journal Letters*, 898, L31
- Nugroho, S. K., Kawahara, H., Gibson, N. P., et al. 2021, *The Astrophysical Journal Letters*, 910, L9
- Patrascu, A. T., Yurchenko, S. N., & Tennyson, J. 2015, *Monthly Notices of the Royal Astronomical Society*, 449, 3613
- Pelletier, S., Benneke, B., Ali-Dib, M., et al. 2023, *Nature*, 1
- Pino, L., Brogi, M., Nascimbeni, V., et al. 2022, *Astronomy & Astrophysics*, 668, A176
- Pino, L., Désert, J.-M., Brogi, M., et al. 2020, *The Astrophysical Journal Letters*, 894, L27
- Quirrenbach, A., Amado, P. J., Ribas, I., et al. 2018, in *Society of Photo-Optical Instrumentation Engineers (SPIE) Conference Series*, Vol. 10702, *Proc. SPIE*, 107020W
- Ramkumar, S., Gibson, N. P., Nugroho, S. K., Maguire, C., & Fortune, M. 2023, *Monthly Notices of the Royal Astronomical Society*, 525, 2985
- Ridden-Harper, A., de Mooij, E., Jayawardhana, R., et al. 2023, *The Astronomical Journal*, 165, 211
- Rothman, L. S., Gordon, I., Barber, R., et al. 2010, *Journal of Quantitative Spectroscopy and Radiative Transfer*, 111, 2139
- Scandariato, G., Borsa, F., Bonomo, A. S., et al. 2023, *A&A*, 674, A58
- Seidel, J., Ehrenreich, D., Allart, R., et al. 2021, *Astronomy & Astrophysics*, 653, A73

- Shulyak, D., Rengel, M., Reiners, A., Seemann, U., & Yan, F. 2019, *Astronomy & Astrophysics*, 629, A109
- Stangret, M., Casasayas-Barris, N., Pallé, E., et al. 2022, *Astronomy & Astrophysics*, 662, A101
- Talens, G., Albrecht, S., Spronck, J., et al. 2017, *Astronomy & Astrophysics*, 606, A73
- Tamuz, O., Mazeh, T., & Zucker, S. 2005, *Monthly Notices of the Royal Astronomical Society*, 356, 1466
- Tennyson, J., Yurchenko, S. N., Al-Refaie, A. F., et al. 2016, *Journal of Molecular Spectroscopy*, 327, 73
- van Sluijs, L., Birkby, J. L., Lothringer, J., et al. 2023, *Monthly Notices of the Royal Astronomical Society*, 522, 2145
- Wende, S., Reiners, A., Seifahrt, A., & Bernath, P. 2010, *Astronomy & Astrophysics*, 523, A58
- Yan, F., Nortmann, L., Reiners, A., et al. 2023, *A&A*, 672, A107
- Yan, F., Pallé, E., Reiners, A., et al. 2022a, *Astronomy & Astrophysics*, 661, L6
- Yan, F., Pallé, E., Reiners, A., et al. 2020, *Astronomy & Astrophysics*, 640, L5
- Yan, F., Reiners, A., Pallé, E., et al. 2022b, *Astronomy & Astrophysics*, 659, A7
- Zechmeister, M., Anglada-Escudé, G., & Reiners, A. 2014, *A&A*, 561, A59

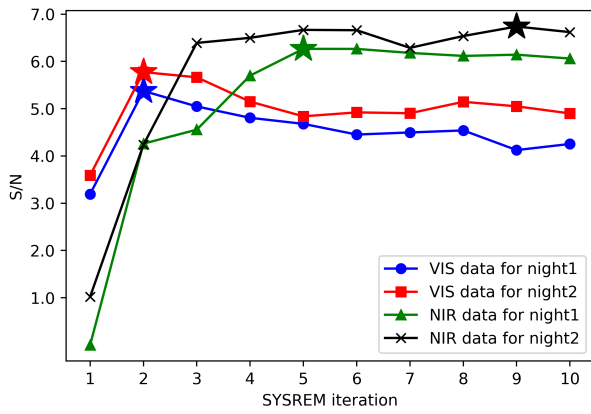


Fig. A.1: Corresponding S/N of Fe I signal at different SYSREM iteration numbers. The maximum S/N values are marked with a star. These S/N values are measured with the peak location where the detection signal is the strongest.

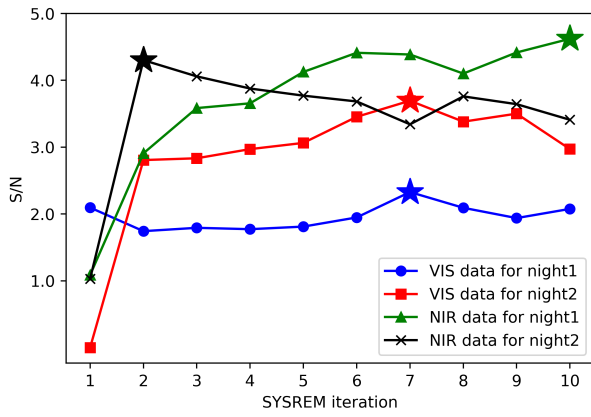


Fig. A.2: Same as Fig.A.1, but for the Ti I signal.

**Appendix A: Additional tables and figures**

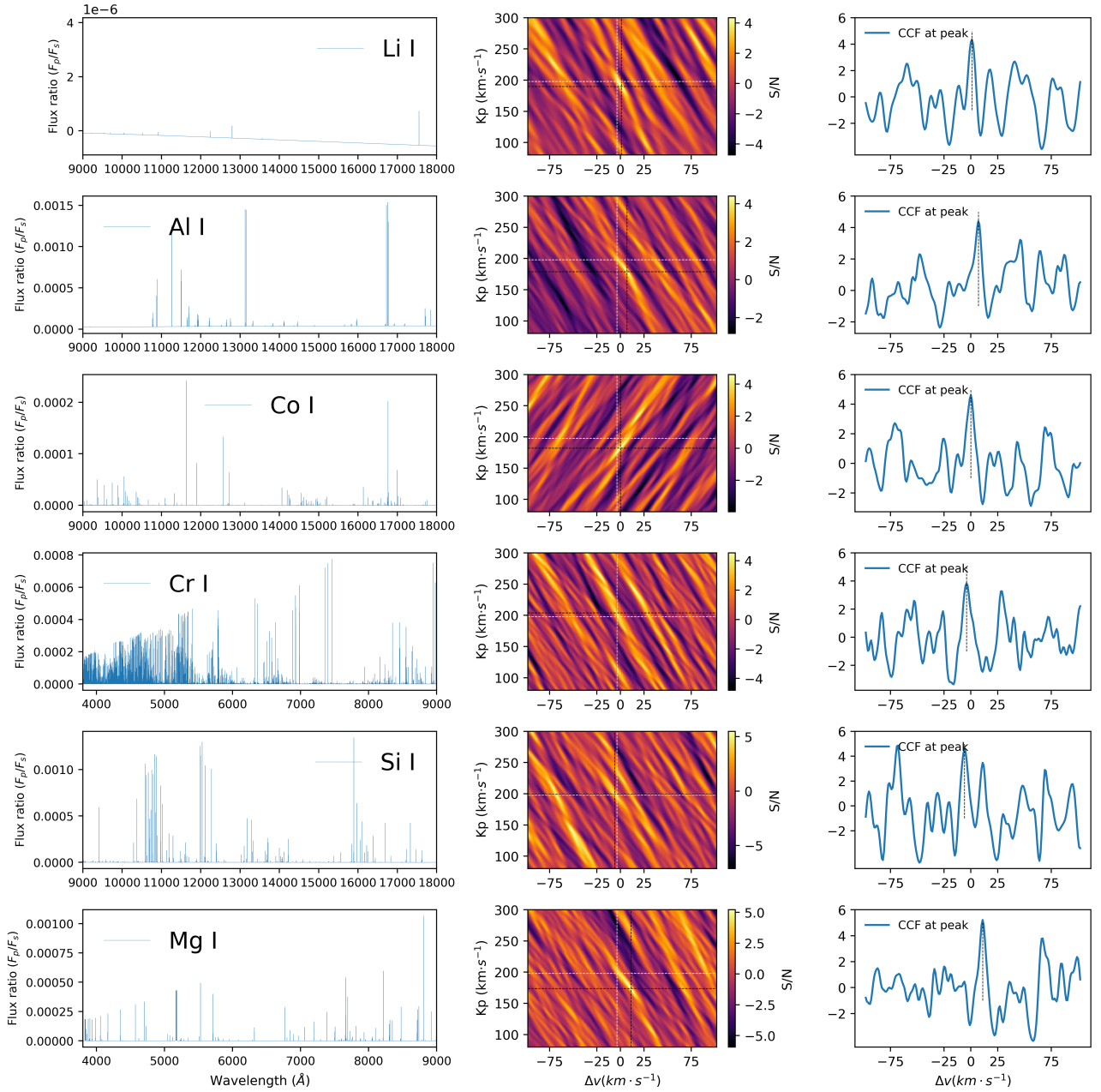


Fig. A.3: Some tentative signals for certain chemical species. Li I, Al I, Cr I, and Si I data were from the NIR spectra of night one, Co I data was from the VIS spectra of night two, and Mg I data was from the VIS spectra of night one. In the middle panel, the dashed white lines indicate the location of the maximum Fe I signal, and the dashed black lines indicate the location where the corresponding chemical species detection significance is at its maximum.

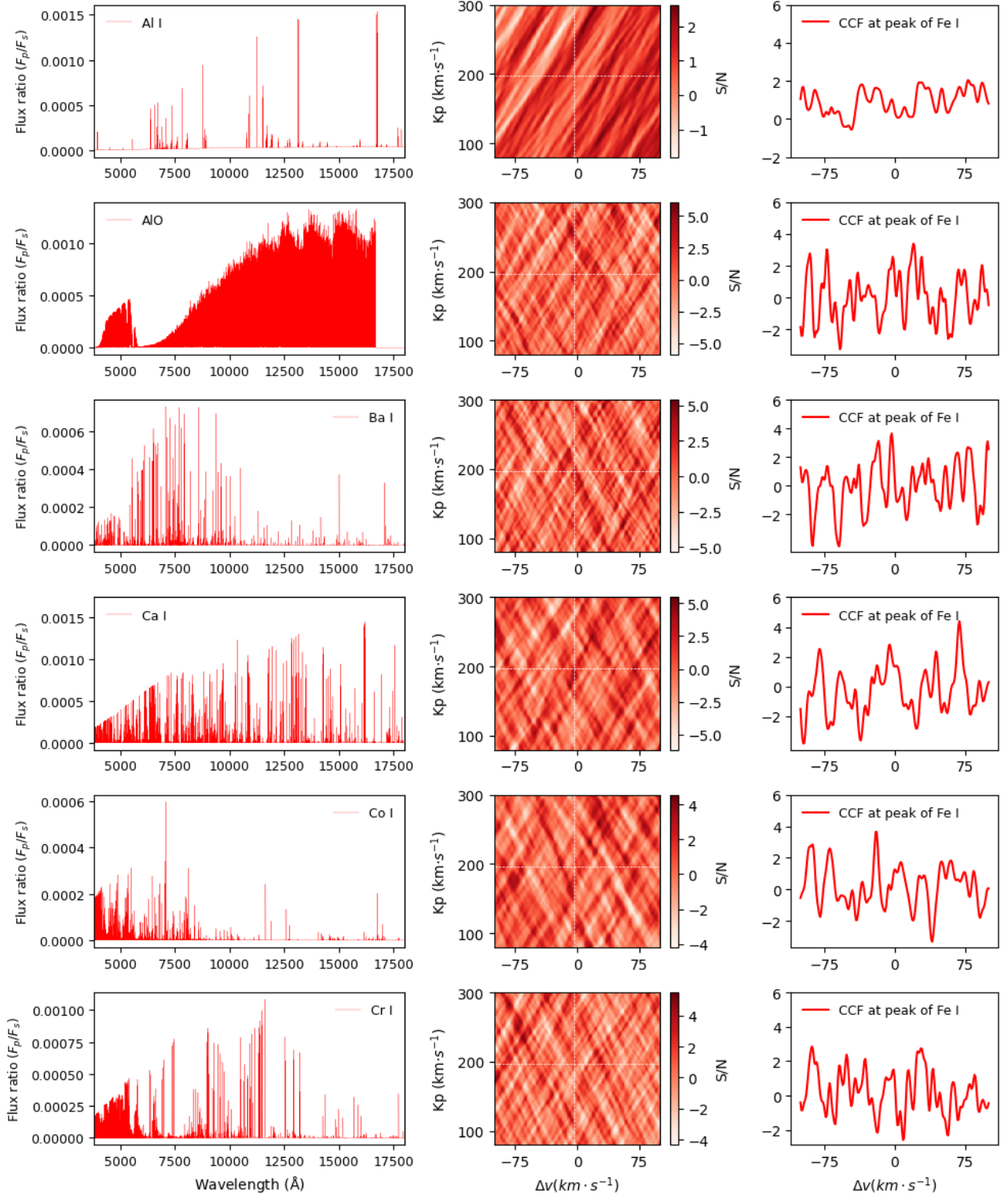


Fig. A.4: Non-detection of other chemical species. *Left panels:* Spectral model of each species. These are normalized spectra that were calculated in a similar way to that described in Sect.3.1. *Middle panels:* Combined two-night S/N maps of each species. The dashed white lines indicate the peak location from the Fe I signal. *Right panels:* CCF at the peak of Fe I.

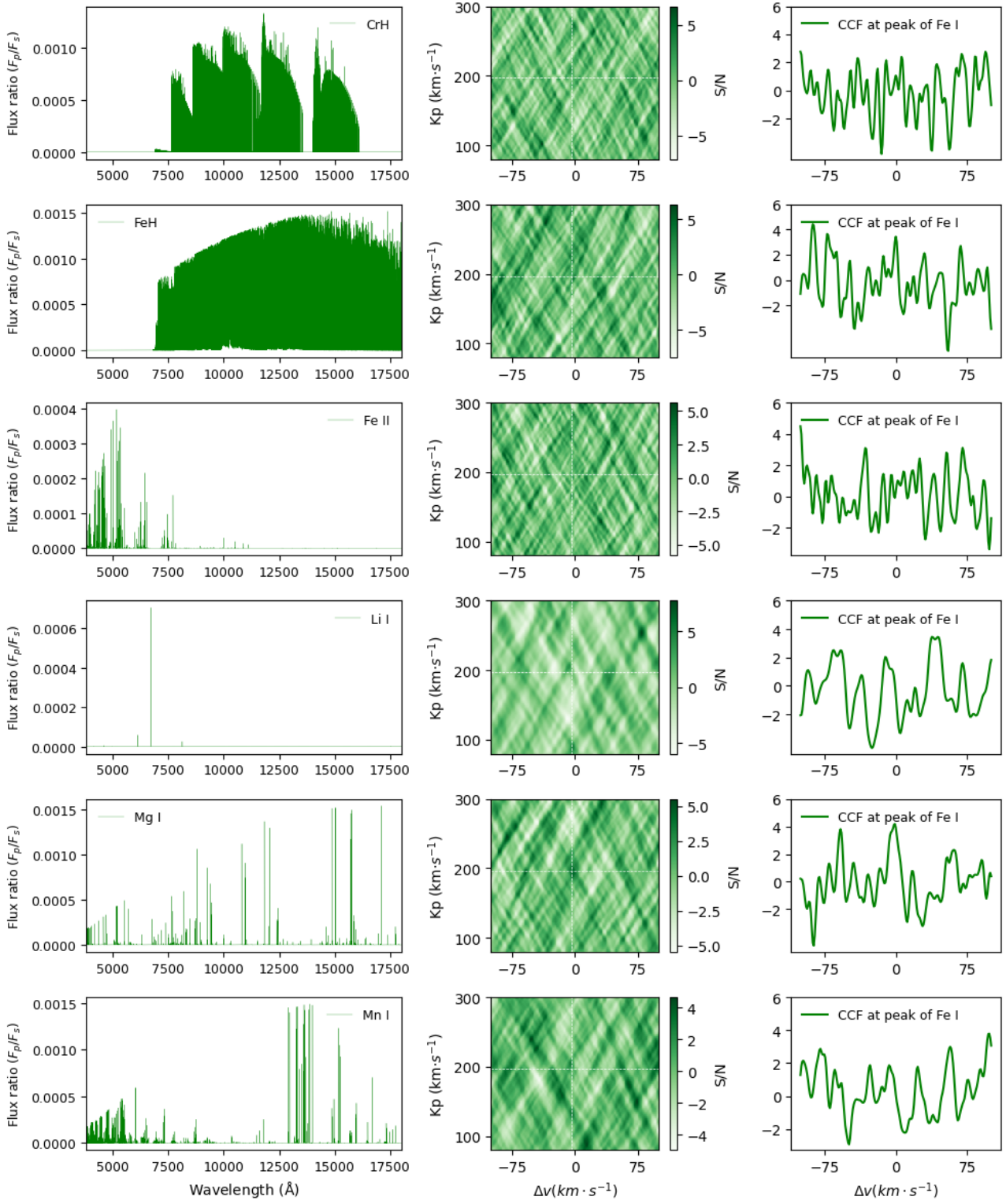


Fig. A.5: Same as Fig.A.4, but for different chemical species.

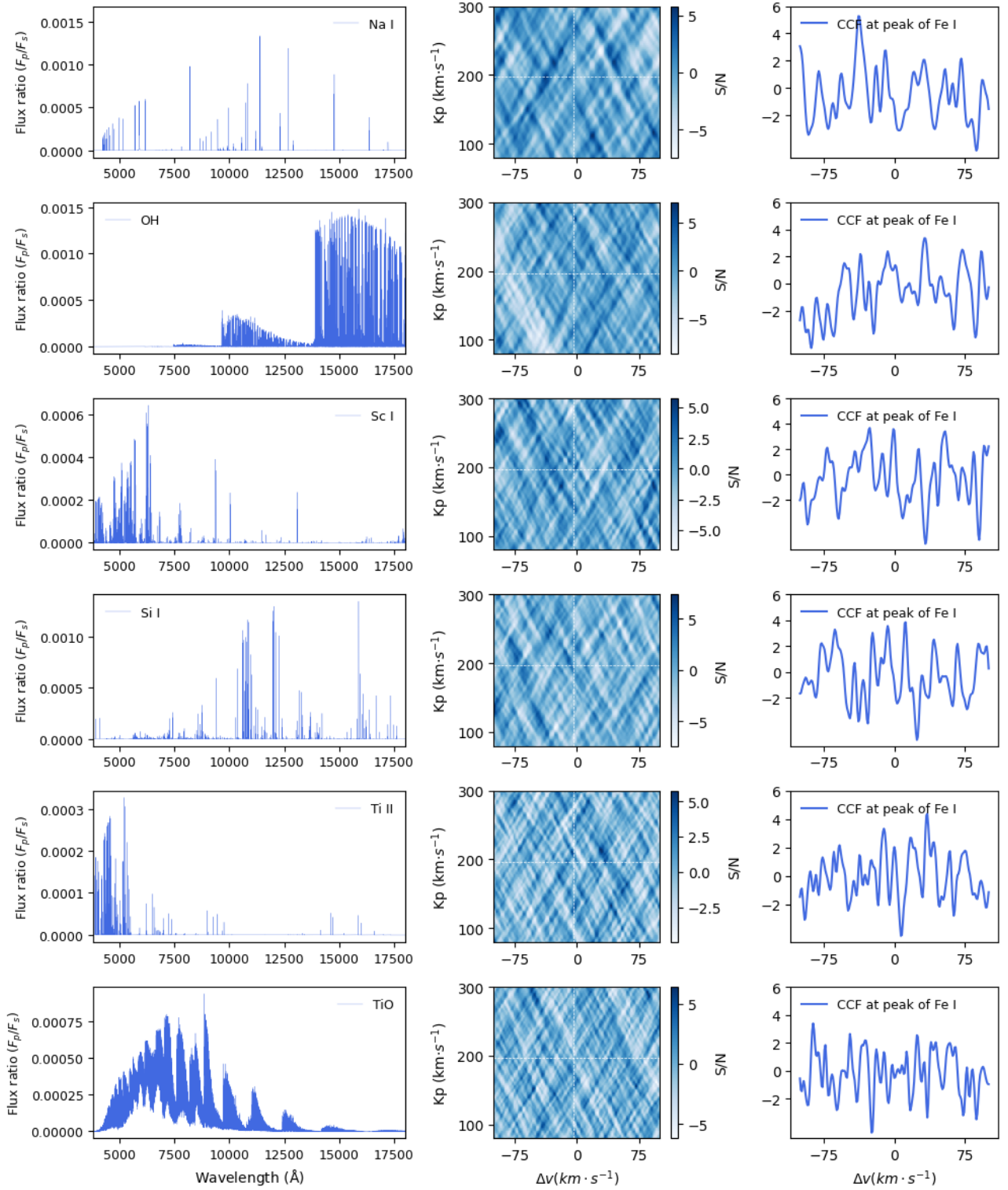


Fig. A.6: Same as Fig.A.4, but for different chemical species.

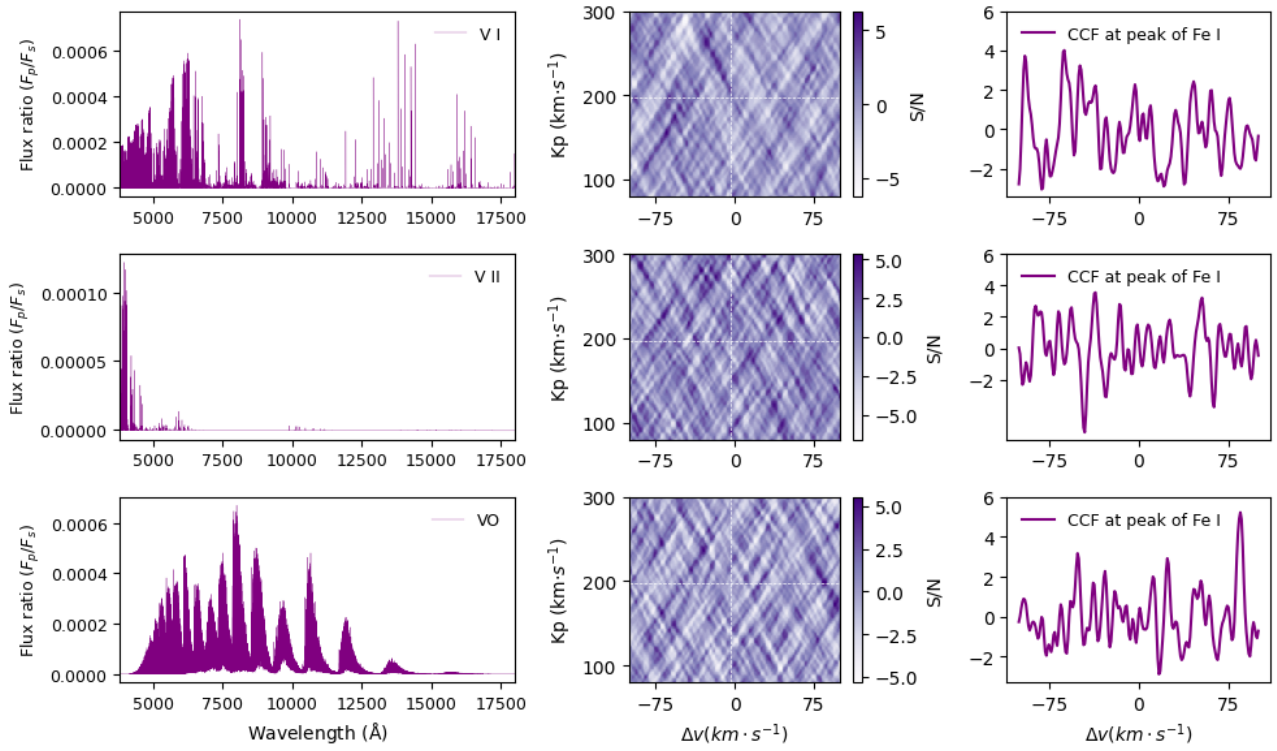


Fig. A.7: Same as Fig.A.4, but for different chemical species.

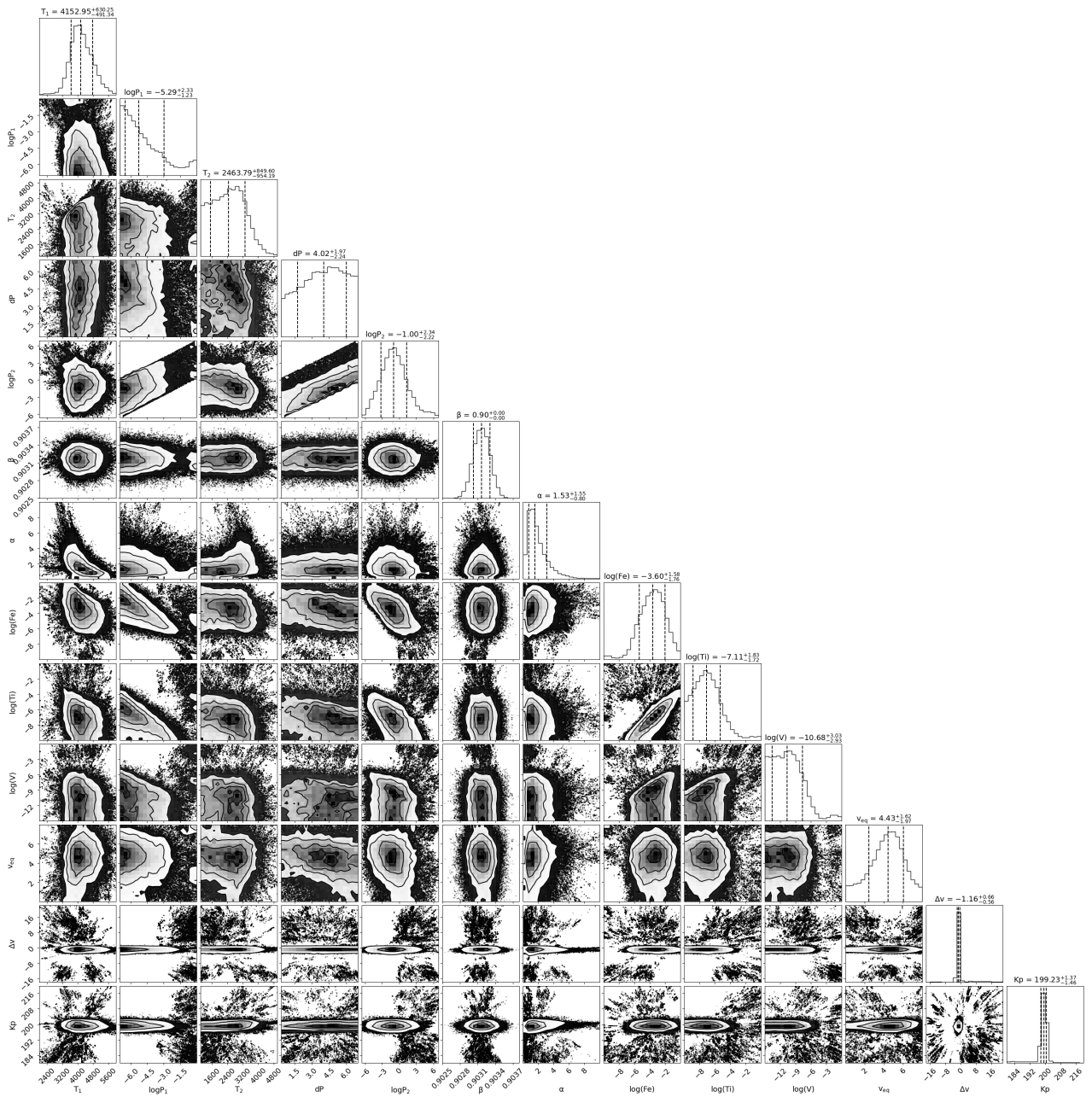


Fig. A.8: Posterior distribution of the parameters from the atmospheric retrieval. Here, the volume mixing ratios of Fe I, Ti I, and V I are assumed to be constant throughout the atmospheric structure.

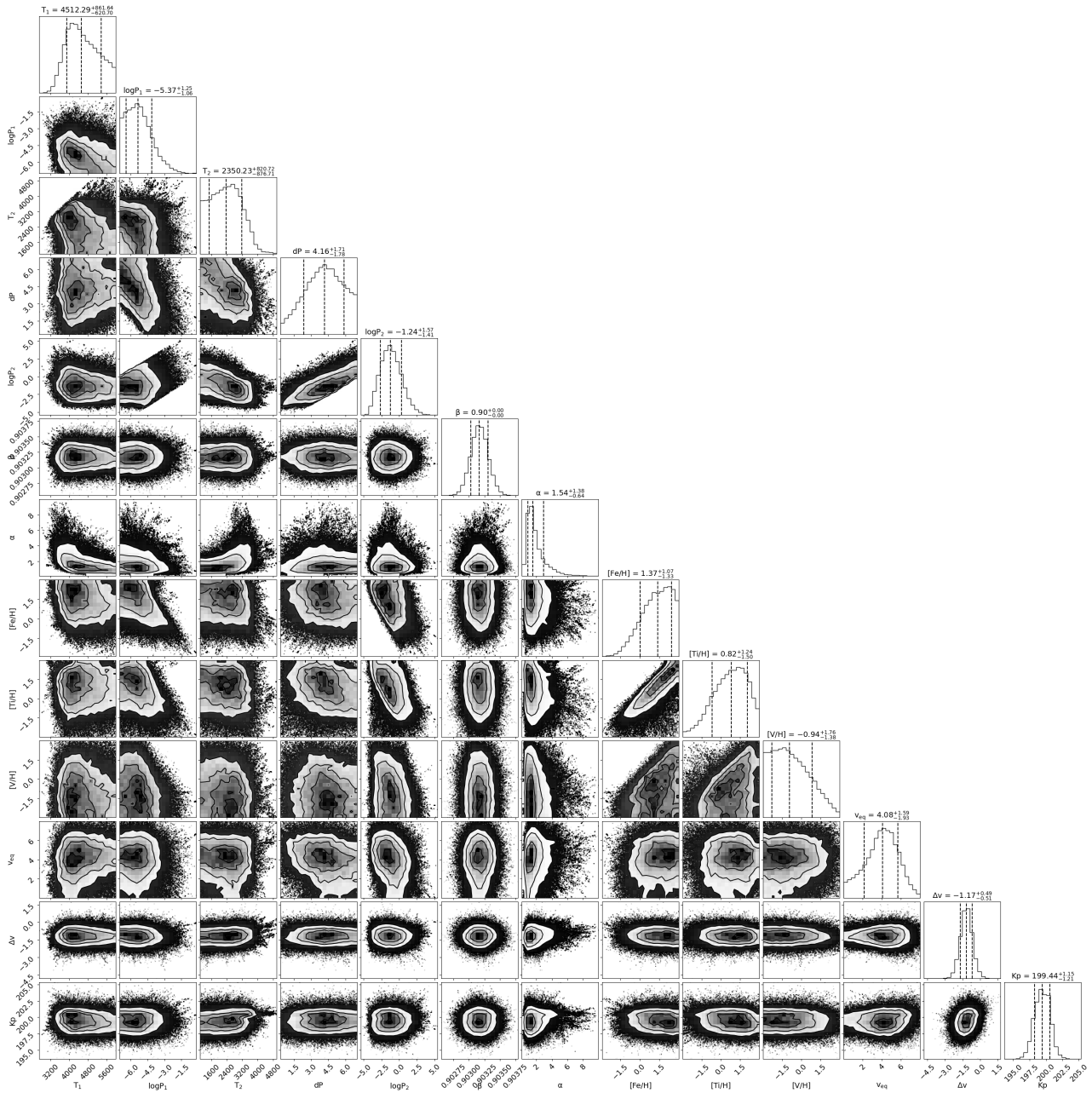


Fig. A.9: Same as Fig.A.8, but the volume mixing ratios of Fe I, Ti I, and V I were calculated with the chemical equilibrium grid.